The Astrophysical Journal Letters, 932:L15 (11pp), 2022 June 20 https://doi.org/10.3847/2041-8213/ac73fe

Onset of Particle Acceleration during the Prompt Phase in Gamma-Ray Bursts as Revealed by Synchrotron Emission in GRB 160821A

Felix Ryde[1], Shabnam Iyyani[2], Björn Ahlgren[1], Asaf Pe'er[3], Vidushi Sharma[1], Christoffer Lundman[1], and Magnus Axelsson[4]
[1] Department of Physics, KTH Royal Institute of Technology and The Oskar Klein Centre, SE-10691 Stockholm, Sweden; fryde@kth.se
[2] Indian Institute of Science Education and Research, Thiruvananthapuram, 695551, Kerala, India; shabnam@iisertvm.ac.in
[3] Department of Physics, Bar-Ilan University, Ramat-Gan 52900, Israel
[4] Oskar Klein Center for CosmoParticle Physics, Department of Physics, Stockholm University, SE-10691 Stockholm, Sweden
Received 2022 February 9; revised 2022 May 19; accepted 2022 May 27; published 2022 June 17

Abstract

The physical processes of gamma-ray emission and particle acceleration during the prompt phase in gamma-ray bursts (GRBs) are still unsettled. In order to perform unambiguous physical modeling of observations, a clear identification of the emission mechanism is needed. An instance of a clear identification is the synchrotron emission during the very strong flare in GRB 160821A, which occurred during the prompt phase at 135 s. Here we show that the distribution of the radiating electrons in this flare is initially very narrow but later develops a power-law tail of accelerated electrons. We thus identify for the first time the onset of particle acceleration in a GRB jet. The flare is consistent with a late energy release from the central engine causing an external shock as it encounters a preexisting ring nebula of a progenitor Wolf–Rayet star. Relativistic forward and reverse shocks develop, leading to two distinct emission zones with similar properties. The particle acceleration only occurs in the forward shock, moving into the dense nebula matter. Here, the magnetization also decreases below the critical value, which allows for Fermi acceleration to operate. Using this fact, we find a bulk Lorentz factor of $420 \lesssim \Gamma \lesssim 770$ and an emission radius of $R \sim 10^{18}$ cm, indicating a tenuous gas of the immediate circumburst surroundings. The observation of the onset of particle acceleration thus gives new and independent constraints on the properties of the flow as well as on theories of particle acceleration in collisionless astrophysical shocks.

Unified Astronomy Thesaurus concepts: Gamma-ray bursts (629)

1. Introduction

Particle acceleration is expected to occur in relativistic, collisionless shocks in gamma-ray bursts (GRBs; Rees & Mészáros 1994; Spitkovsky 2008). However, many aspects of the acceleration mechanism are not yet fully understood. Such aspects include the microphysical processes that mediate the acceleration of electrons, the physical conditions for such a process to become efficient, and the fraction of electrons that undergo acceleration. While synchrotron emission from the external shock during the GRB afterglow reveals the power-law distribution of shock-accelerated particles (Tavani 1996; Wijers & Galama 1999), the situation for the prompt phases is less certain. Most prompt spectra have an exponential cutoff above their peak (Goldstein et al. 2012; Yu et al. 2019), which indicates that any particle acceleration is inefficient. On the other hand, some spectra have a prominent high-energy power law above their peak (e.g., Abdo et al. 2009; Axelsson et al. 2012). At the same time, much evidence points toward both synchrotron and emission from the jet photosphere contributing to varying degrees during the first few 100 s of a GRB emission (Mészáros et al. 2002; Ajello et al. 2019; Li 2020). In contrast to the synchrotron spectrum, photospheric emission spectra probe radiation-mediated shocks (Beloborodov 2017; Samuelsson et al. 2022) and therefore are related to a different physical setting. Thus, correctly identifying the emission mechanism as being synchrotron is necessary to be able to identify and study any particle acceleration.

During the intense burst GRB 160821A (Sharma et al. 2019), synchrotron emission is clearly identified because it has a broad, nonthermal spectrum with several breaks, at around 100 keV, 1000 keV, and 50,000 keV, which characterize the synchrotron spectra of other GRBs (Ravasio et al. 2019; Oganesyan et al. 2017; Acuner & Ryde 2018). The main emission also occurs later than 100 s after the trigger and has a long duration, which supports a synchrotron interpretation (Oganesyan et al. 2019; Li 2020). Other facts in support of synchrotron emission are its high degree of polarization (>60%, in the energy range 100–300 keV) (Sharma et al. 2019; Gill et al. 2020) and that it is very bright (Oganesyan et al. 2017; Acuner & Ryde 2018). In this paper, we therefore use synchrotron spectral fits of the prompt emission in GRB 160821A to study the distribution of the radiating electrons.

The observed synchrotron emission is powered by energy dissipation in shocks, where the electrons are heated and cool rapidly in a local magnetic field B (Rees & Mészáros 1994). The electrons assume a quasi-Maxwellian energy distribution around a Lorentz factor γ_m corresponding to some fraction of the available dissipated energy. If the conditions are right, the electrons can be further accelerated in the shocks (Sironi & Spitkovsky 2011), forming a power-law distribution with an index $p \sim 2.2$ –2.5, extending to higher energies ($N_{el}(\gamma)d\gamma \propto \gamma^{-p}$, above γ_m). Because the episode analyzed here is very bright the emission has to be very efficient, which corresponds to the cooling time of the radiating electrons having to be shorter than the typical dynamical time, this will cause a distribution of cooled electrons $N_{el}(\gamma)d\gamma \propto \gamma^{-2}$ below

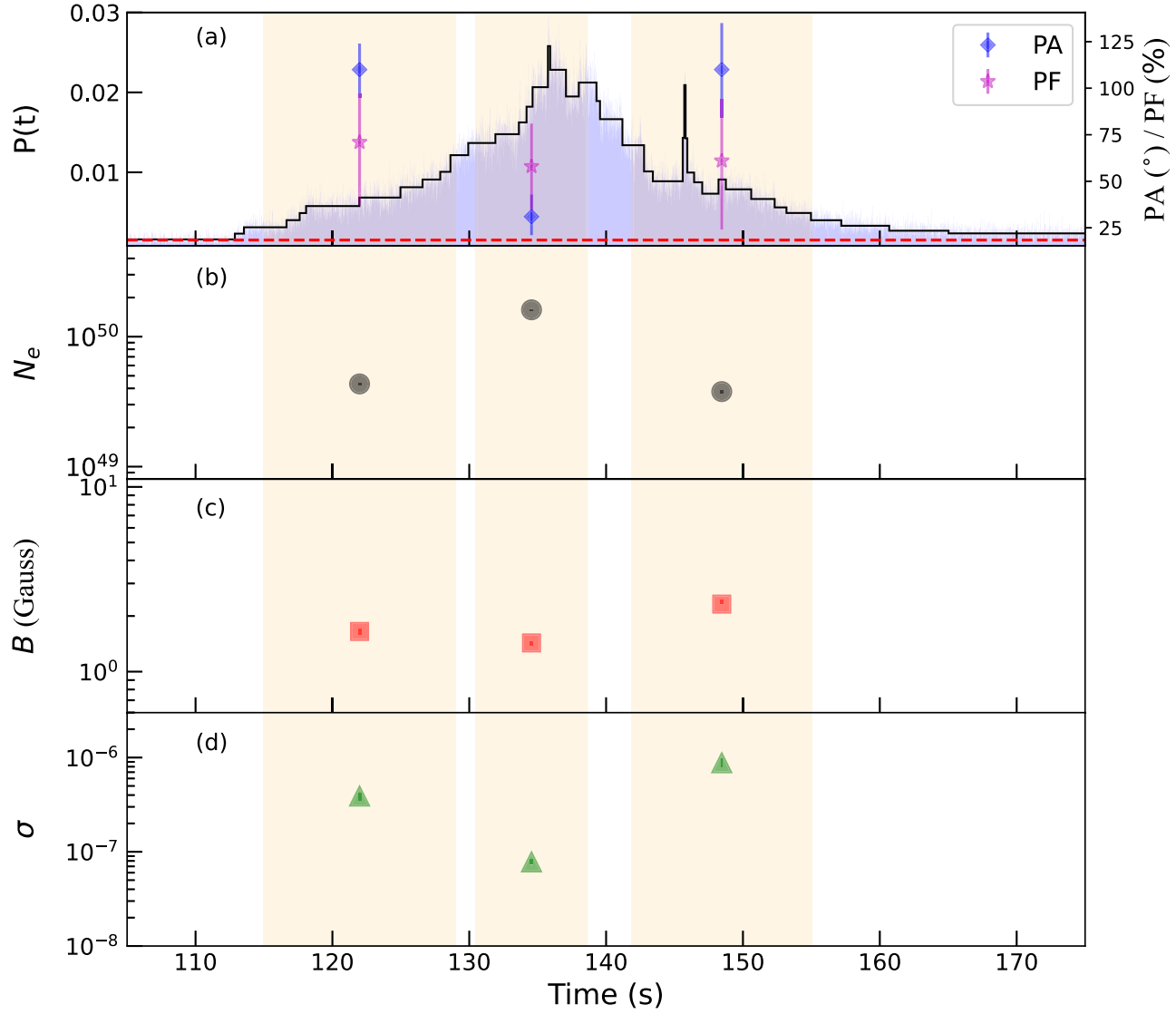

Figure 1. Evolution of the main episode of GRB 160821A. The yellow shaded regions represent the three time bins that are analyzed and correspond to time intervals where the polarization measurements are made using AstroSat CZTI data. (a) The high-resolution (0.01 s) light curve (blue) and the Bayesian block binned light curve (black line), with a false-alarm probability to compute the prior, $p_0 = 0.01$. The y-axis represents the probability density, which gives the counts per bin divided by the width of the bin. The polarization fraction, PF, and the polarization angle, PA, obtained by Sharma et al. (2019) are shown in magenta star and blue diamonds, respectively. The temporal variation of the derived physical parameters, assuming $\Gamma = 300$ and $z = 0.4$, are shown: (b) the number of radiating electrons, N_e; (c) the comoving magnetic field, B, and (d) the magnetization, σ.

γ_m down to a Lorentz factor of γ_c, depending on the magnetic field strength. Moreover, any high-energy power law of accelerated electrons will become steeper by unity, to an index of $p + 1$ (e.g., Sari et al. 1998). As the electrons radiate, the observed synchrotron photon spectrum will have corresponding power-law segments with breaks at energies $h\nu_c$ and $h\nu_m$.

2. Synchrotron Spectral Fits of the Strong Flare in GRB 160821A

GRB 160821A was observed by several space observatories, among others AstroSat (Bhalerao et al. 2016) and the Fermi gamma-ray space telescope (Stanbro & Meegan 2016) (hereafter Fermi). It is the third brightest GRB observed by Fermi in terms of energy flux observed in the energy range 10–1000 keV. The observed prompt emission of GRB 160821A consists of two emission episodes where the first emission episode extends for a period of 112 s from the time of trigger, and the second emission episode peaks at around 135 s, lasting for around 40 s and is nearly a hundred times brighter than the first emission episode (Figure 1). Here, we focus the study on this intense flare, i.e., the second episode. For the spectral analysis, we choose the data ranging between roughly 8 keV and 40 MeV from the Fermi Gamma-ray Burst Monitor (GBM) including sodium iodide (NaI) and bismuth germanate (BGO) detectors (NaI6, NaI7, NaI9, BGO 1; Meegan et al. 2009). In addition, the Large Area Telescope Low-Energy (LAT-LLE) and LAT data in the energy ranges of 30–130 MeV and 100 MeV–5 GeV, respectively, are also used for the spectral analysis (Atwood et al. 2009). The same spectral files generated for the time-resolved spectroscopy in Sharma et al. (2019) are used for this study. The effective area correction factors estimated in that study for the different detectors with respect to BGO 1, whose value was fixed to unity, are the following: 0.97 ± 0.01 for n6, 0.92 ± 0.01 for n7, 0.94 ± 0.01

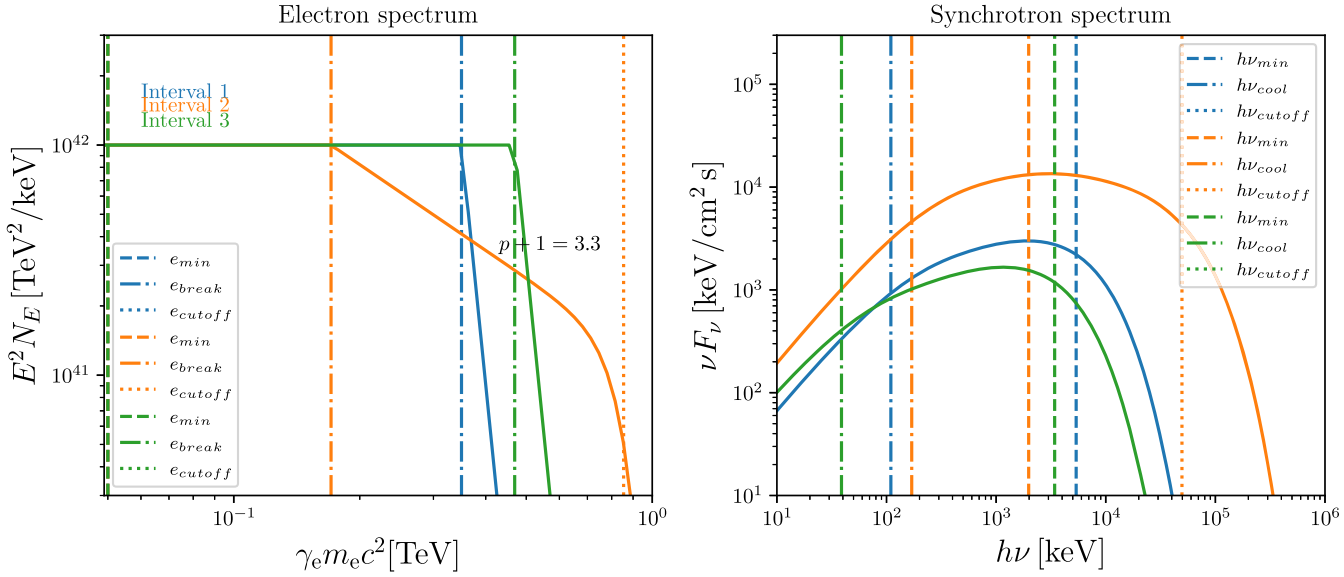

Figure 2. Spectral distributions of electrons and gamma rays. Left panel: electron energy spectrum used in fits to the three time intervals. Because the fits are translationally degenerate, the energy scale is arbitrary (see, e.g., Burgess et al. 2014). The physical quantities are later derived in Appendix A.3. Right panel: νF_ν spectrum from the three time intervals, being the best fits to the data.

Table 1
Measured Spectral Properties Using the Synchrotron Emission Model

Time Intervals	$h\nu_c$ (keV)	$h\nu_m$ (keV)	$h\nu_{\rm cutoff}$ (keV)	$F_\nu(h\nu_c)$ (cm^{-2} s^{-1})	$p+1$
Interval 1	$108.3^{+11.8}_{-12.3}$	$5.5^{+1.0}_{-0.9} \times 10^3$		$8.5^{+0.1}_{-0.1}$	
Interval 2	$167.4^{+14.2}_{-12.4}$	$2.3^{+1.1}_{-1.0} \times 10^3$	$5.2^{+1.9}_{-1.7} \times 10^4$	$27.2^{+0.3}_{-0.4}$	3.3 ± 0.2
Interval 3	$38.8^{+5.2}_{-5.6}$	$3.4^{+1.1}_{-0.9} \times 10^3$		$10.4^{+0.2}_{-0.2}$	

Note. The values correspond to the means of the respective marginalized posterior distributions. The intervals denote Bayesian credible intervals corresponding to the 95% highest density interval.

for n9, and 0.84 ± 0.06 for LAT. The spectral analysis is carried out in the Multi-Mission Maximum Likelihood (3ML) software (Vianello et al. 2015), wherein the synchrotron emission model (Aharonian et al. 2010) is implemented using the NAIMA package (Zabalza 2015).

We divide the light curve of the main episode into three time bins, shown in the uppermost panel of Figure 1. This division follows the one made for the polarization measurement of Sharma et al. (2019). They further showed that the spectral shapes are different but relatively steady within these three intervals. This fact further motivates using the integrated signal during the intervals. Each time bin is fitted with a synchrotron spectrum, using Bayesian analysis, with priors on the free parameters as described in Appendix A. The right-hand panel in Figure 2 shows the best-fit power spectrum (νF_ν) for the three time intervals. In each interval, we thus determine the synchrotron cooling frequency, $h\nu_{\rm c}$, and the synchrotron frequency of the injected electrons, $h\nu_{\rm m}$. In interval 2 we also identify a high-energy cutoff at $h\nu_{\rm cutoff}$ and the high-energy power-law index. The parameter values are given in Table 1. The left-hand panel in Figure 2 shows the corresponding energy distribution of the radiating electrons. In Appendix A we further show the fitted spectra in count space (Figure 3), as well as the corner plot of all the fitted parameters, $\gamma_{\rm m}$, norm, and p (Figure 4).

We identify a few important spectral changes between the fits of the three time bins. While the first and third intervals are rather similar, the spectral shape of the second interval differs significantly. First, the ratio $\gamma_{\rm m}/\gamma_{\rm c}$ is much smaller; second, a clear power-law distribution above $\gamma_{\rm m}$ is formed with $p = 2.3$; and third, the flux level is the largest. It is interesting to note that the variations detected in interval 2 coincide with the change in polarization degree (Sharma et al. 2019). The main conclusion from this spectral analysis is therefore that something happens in interval 2 that is responsible for the onset of particle acceleration.

3. Scenario Derived from the Observations

Because the flare is very bright, it has to have originated in an external shock, as any internal shocks are too inefficient (Kobayashi et al. 1997; Beloborodov 2000; Spada et al. 2000; Kobayashi & Sari 2001). Furthermore, it cannot either be a collision between a late emitted shell that catches up to a shell from an early ejection by the GRB. At the collision time of $\sim$100 s, both shells have to be relativistic and the relative Lorentz factor between the colliding shells would therefore be low. A large contrast in Lorentz factors is needed to explain the exceptional brightness of the flare. Moreover, the main emission episode cannot be part of the long-lived, self-similar afterglow emission. The reason is that an additional high-energy component emerges at the end of the main emission episode and appears as a separate spectral component at around 185 s (Sharma et al. 2019). This component is strongly required

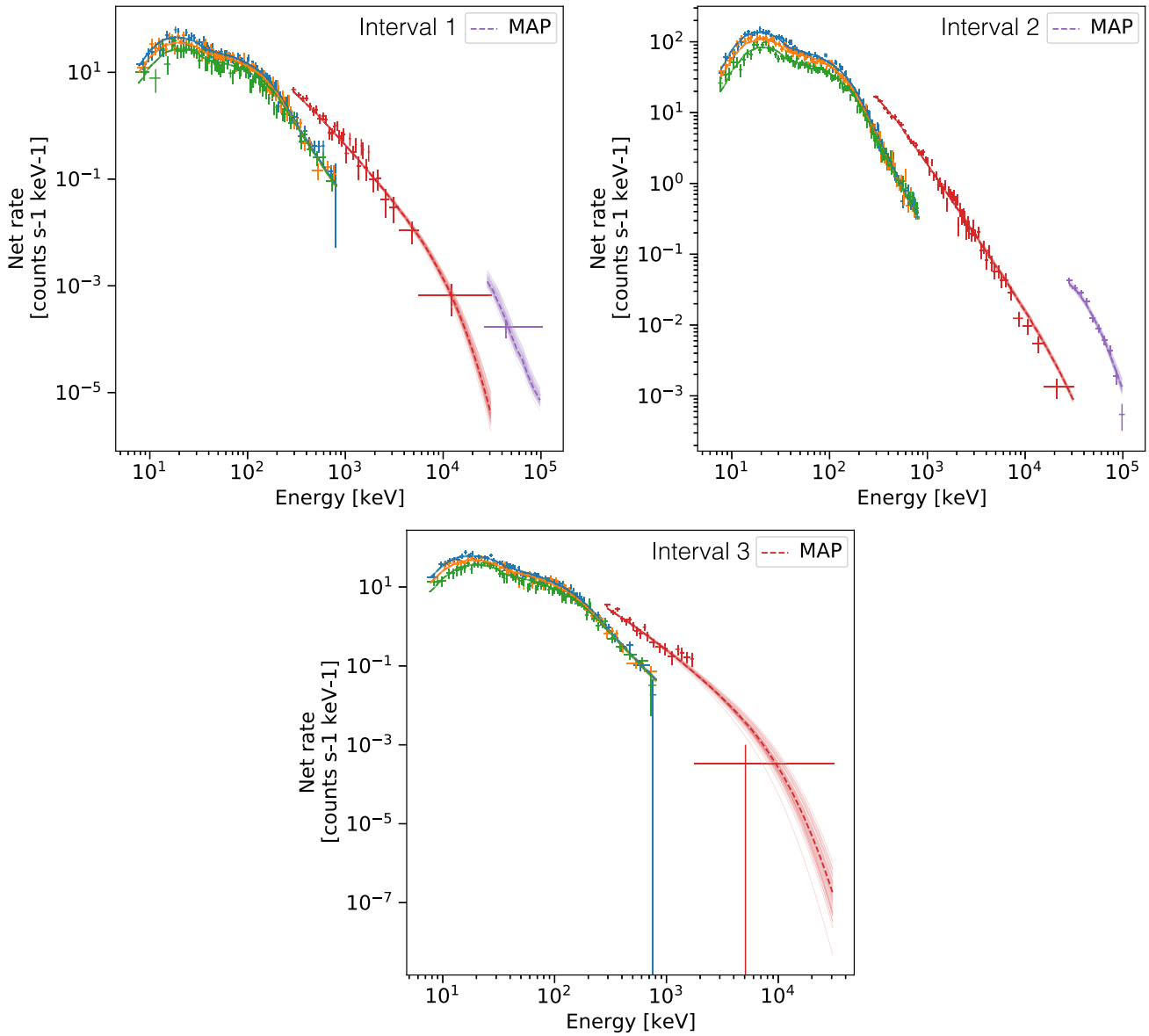

Figure 3. Draws from the posterior distribution of the model conditioned on the data in the three intervals. The 50 thin lines correspond to random draws from the posterior distribution, and the dashed line corresponds to the MAP. The data and model have been rebinned to bins containing at least 20 counts. The blue, orange, green, red, and purple colors correspond to the NaI6, NaI7, NaI9, BGO 1, and LAT/LLE data, respectively.

by the data and gives a change in the Akaike Information Criterion (AIC) of 116. In addition, significant emission above 100 MeV from this component was observed by Large Area Telescope (LAT) on board Fermi for a period of ∼2000 s after the Gamma-ray burst monitor (GBM) trigger time (T_0), decaying as a power law in time with the temporal index of 1.15 ± 0.10 in the Fermi/LAT energy range. The additional, long-lived component is thus naturally related to the afterglow, produced by an external shock in the self-similar blast-wave regime (Ajello et al. 2019). The onset of the afterglow emission at $t \sim 185$ s indicates a deceleration radius that is larger than the emission radius of the main episode, which peaks at 135 s. The conclusion is therefore that the main emission episode must be due to a blast wave that encounters a dense circumburst shell that is, at most, mildly relativistic, lying within the deceleration radius. As this encounter occurs already at ∼130 s, such a shell, therefore, needs to be a preexisting structure because any earlier GRB ejection would still be relativistic at that time. A plausible origin of such a preexisting structure is the ring nebulae around the progenitor Wolf–Rayet stars (WR). These nebulae are either caused by massive winds, which sweep up the circumstellar medium, or by instabilities that cause elevations of the outer envelope, leading to occasional giant-eruption events, with major mass ejections (Chu 1981; Crowther 2007). Such events are thought to cause narrow, nearly spherical shells around the progenitor star (Johnson & Hogg 1965). Up to a third of WR stars observed in the galaxy have a narrow ring nebula (Marston 1997) lying at a typical distance of 1 pc from the central star, and some have much smaller sizes (Stock & Barlow 2010). The existence of a low-density cavity within such wind-blown bubbles (Toalá & Guerrero 2013) would lead to very little interaction with the blast wave before it encounters the circumstellar ring itself. This fact is supported by the quiescent period observed just before the 130 s flare in GRB 160821A.

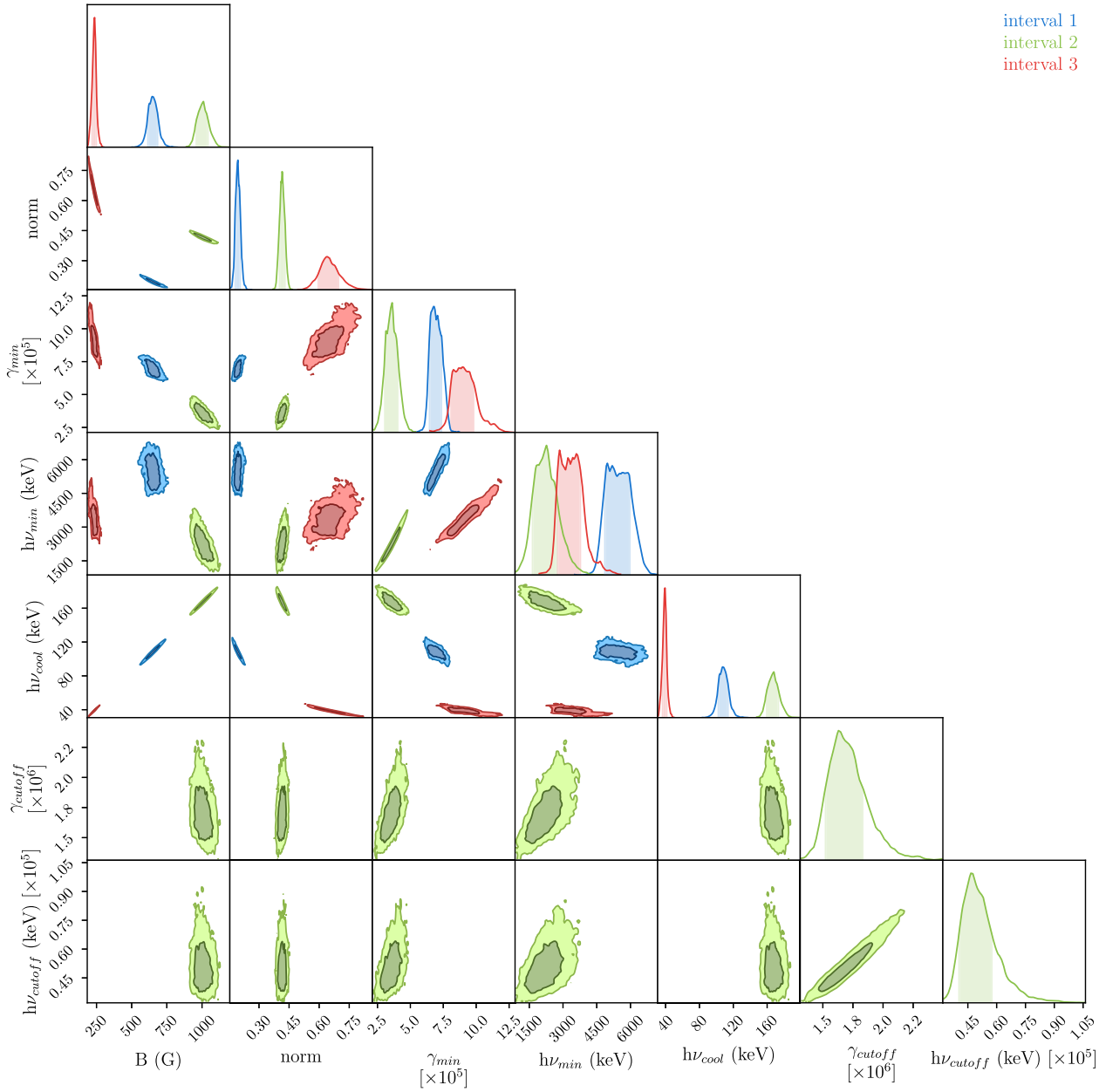

Figure 4. Corner plot of the posterior probability distribution of free model parameters, as well as the derived values of the break energies in the photon spectra. The blue, green, and red colors correspond to intervals 1, 2, and 3, respectively, and the light and dark contours represent the 68% and 95% credible regions.

Finally, the ratio of pulse width to pulse time for the main episode is $40\,\mathrm{s}/135\,\mathrm{s} < 1$, which indicates late central engine activity (Lazzati & Perna 2007; Pereyra et al. 2021) causes an external-shock flare. This is reminiscent of strong gamma-ray flares observed at the end of the prompt phase (Zhang et al. 2018) and X-ray flares observed after the prompt activity in the gamma-ray band (Hu et al. 2014), which all require a long-lived central engine activity.

Within this scenario, the synchrotron spectra from the analysis above can be translated into physical properties of the plasma. Because both the bulk Lorentz factor and the redshift are unknown, we initially use the fiducial value of $\Gamma = 300$ and the estimated value of $z = 0.4$ (see Appendix A.2). The physical properties are derived in Appendix A.3. Table 2 gives the derived values of γ_c; γ_m; *B;* the emission (dynamical) radius $R_{\rm dyn} = 2c\,\Gamma^2\,\Delta t$, where Δt is the pulse duration; the total number of radiating electrons N_e; and finally, the magnetization, $\sigma = B'^2/4\pi\Gamma n' m_p c^2$. Here, the primed quantities are in the comoving frame and n' is the particle density. The magnetization is, therefore, determined for the downstream of the shock. The typical Lorentz factor of the electrons is found to be very high, $\gamma \sim 10^5$. Its value is given by $\gamma \sim \epsilon_e(m_p/m_e)\Gamma$, where Γ is the relative Lorentz factor between the colliding shells, m_p and m_e are the proton and electron masses, and ϵ_e is the energy partition fraction. The high value of γ is therefore consistent with the external-shock scenario and a large contrast in Lorentz factors.

There are three main changes in the physical properties between the first and second episode: (i) The number of emitting particles, N_e, increases by a factor of 4. (ii) There is an onset of particle acceleration to a power law with $p = 2.3$, which contains around 10% of the particles. (iii) The

Table 2
Derived Physical Parameters, Based on the Assumption that the Observer Frame Cooling Time, $t_{\rm cool}$ is the Same for All Intervals

Time Intervals	$\gamma_{\rm c}$ (10^5)	$\gamma_{\rm m}$ (10^5)	B (Gauss)	$R_{\rm dyn}$ (10^{17} cm)	N_e (10^{49})	σ (10^{-7})
Interval 1	$1.33^{+0.09}_{-0.10}$	$9.4^{+0.8}_{-0.8}$	$1.65^{+0.06}_{-0.06}$	2.2	$4.33^{+0.09}_{-0.09}$	$3.9^{+0.3}_{-0.4}$
Interval 2	$1.78^{+0.10}_{-0.09}$	$6.5^{+1.2}_{-1.2}$	$1.43^{+0.03}_{-0.04}$	〃	$16.1^{+0.2}_{-0.2}$	$0.78^{+0.05}_{-0.05}$
Interval 3	$0.67^{+0.06}_{-0.07}$	$6.3^{+0.8}_{-0.8}$	$2.32^{+0.12}_{-0.09}$	〃	$3.78^{+0.10}_{-0.11}$	$8.8^{+1.1}_{-1.0}$

Note. The fiducial value of $\Gamma = 300$ and $z = 0.4$ are assumed. The intervals denote Bayesian credible intervals corresponding to the 95% highest density interval.

magnetization σ decreases. At the same time, the B field does not change very much, while $\gamma_{\rm m}$ and $\gamma_{\rm c}$ are the same to within a factor of 2. We note that there is a small but significant decrease in $\gamma_{\rm m}$ by 30%. From a theoretical point of view, both the fraction of particles that have been accelerated in interval 2 ($\sim$10%) and the power-law slope of the injected electrons ($p \sim 2.3$) are in line with the robust expectations for particle acceleration in weakly magnetized flows (Sironi et al. 2015). The high-energy cutoff during interval 2 is at around 50 MeV (Table 1). Such a cutoff is expected from shock acceleration and depends on many factors, such as the shock duration (Kirk & Reville 2010; Sironi et al. 2013) and magnetic field configuration (Lemoine 2013).

The observed increase in emitting particles during interval 2 can have different reasons. In the encounter between the blast wave and the slow-moving and dense preexisting shell, relativistic forward and reverse shocks will develop, leading to two distinct emission zones. The properties of these shocks are expected to be similar because the slow shell is preexisting (Pe'er et al. 2017). The forward shock is pronounced during interval 2, as it moves through the denser shell and accelerates its particles across the shock into a power-law distribution. Intervals 1 and 3 are then related to a reverse shock moving into the blast wave and heating its particle content. Alternatively, the observed emission is only from the forward shock that encounters fluctuation in the particle density in the preexisting shell. In both cases, the denser regions cause a larger release of energy, leading to the change in the observed intensity. Moreover, the increase in particle density is expected to slightly decrease $\gamma_{\rm m}$ (Pe'er & Wijers 2006). This is largely similar to what is observed. Finally, as the B fields are relatively constant, the increase in emitting particles also explains the observed decrease in magnetization, σ.

4. Onset of Particle Acceleration

The onset of particle acceleration can therefore naturally be related to the variation in magnetization. We find that σ in GRB 160821A decreases by a factor of 5 in interval 2 and then increases again by a factor of 10. It might thus have dropped below a critical value for acceleration to become operative during interval 2. One possibility that is directly related to the magnetization at a relativistic shock is the finding that the microturbulence centers (e.g., caused by Weibel instabilities) needed for Fermi acceleration to operate cannot be formed if the magnetization exceeds a certain critical value (Lemoine & Pelletier 2011; Lemoine 2013). Analytical work and numerical simulations (Sironi & Spitkovsky 2011; Lemoine et al. 2013; Pelletier et al. 2017) show that the theoretical value of the critical magnetization is $\sigma_{\rm c} \sim 10^{-6}$ (assuming $\Gamma = 300$). This value is, however, consistently larger than what is found during the main episode in GRB 160821A, which has a magnetization $\sigma \sim 10^{-7}$ (Table 2), indicating that particle acceleration ought to appear throughout its duration. On the other hand, as shown in Appendix B, a viable solution[5] exists for larger values of the Lorentz factor, $450 \lesssim \Gamma \lesssim 820$, which corresponds to shock radii at $R \sim 10^{18}$ cm. In such a case, the magnetization drops below the critical value as stipulated. We note, however, that such large values of Γ and R require very low particle densities of the circumburst medium (e.g., Rees and Mészáros 1992). With the average value of $\Gamma = 595$ from the range above, the particle density required is as low as $\sim 10^{-3}\,{\rm cm}^{-3}$, which indicates a tenuous gas of the immediate burst surroundings. On the other hand, $R = 10^{18}$ cm is the typical size of WR ring nebulae, which, combined with the low densities of their interiors, makes the large values of R and Γ consistent with the scenario presented above in Section 3. If indeed the onset of particle acceleration is caused by Fermi acceleration and determined by the survival of microturbulent magnetic fields (Lemoine & Pelletier 2010), then the observed transition from acceleration to nonacceleration gives a new, independent way to constrain the bulk Lorentz factor.

Another possibility for the observed particle acceleration is the converter acceleration mechanism (Derishev et al. 2003). In this mechanism, $e^{\pm}$ pairs in the upstream gain energy as they cross the shock front. The energetic electrons then cool by inverse Compton emission in the downstream, producing energetic photons, which can propagate back across the shock to the upstream. If the opacity for photon–photon interaction is high enough, $e^{\pm}$ pairs can again be created in the upstream, thereby completing a Fermi cycle. The converter mechanism is very efficient (Derishev & Piran 2016) but there are many mechanisms that can counteract it (Derishev 2017). For instance, the relative efficiency of inverse Compton emission will change depending on the magnetic field strength, which can lead to synchrotron losses becoming dominant. A change in the Lorentz factor jump across the shock front will also affect its efficiency. If the power-law distribution of electrons observed in GRB 160821A is due to the converter mechanism, then the onset of particle acceleration must be caused by an increase in its efficiency, causing it to become operational. Neither a change in magnetic field strength nor a change in Lorentz factor jump is, however, expected in the scenario described above in Section 3.

[5] A comparison between Tables 2 and 4 also illustrates the sensitivity of the derived parameter values to the assumed value of the Lorentz factor, Γ. Most of the derived parameters only weakly depend on z (see Appendix A.3), apart from N_e and σ, which vary by around a factor of 5 between $z = 0.4$ and $z = 1.0$.

5. Discussion and Conclusion

We have analyzed the gamma rays in GRB 160821A, which can be convincingly identified as synchrotron emission. Synchrotron modeling of the observed data consequently reveals the energy distribution of the radiating electrons. We find for the first time evidence for the onset of the acceleration process, in which a fraction of thermally distributed particles is accelerated into a power-law distribution to higher energies. We argued that the strong flare in GRB 160821A is due to an interaction between a late blast wave interacting with a preexisting shell of slowly moving material, such as a WR ring nebulae. This causes forward and reverse shocks, both of which are relativistic and have similar properties (Pe'er et al. 2017). The particle acceleration detected in interval 2 occurs in the forward shock, which encounters a denser region and lower magnetization.

The high degree of polarization observed during the main episode indicates that the jet should carry a dominant ordered magnetic field component in a scale larger than Γ^{-1} or a globally ordered toroidal field (Sharma et al. 2019). In addition, a consequence of particle acceleration is that a shock-generated, small-scale, random B field is formed (Keshet et al. 2009). Therefore, such a field should exist in addition to the ordered field during interval 2 in GRB 160821A. The combination of these field components can change the resulting weight of the polarization contributions over the jet image, thereby altering the observed polarization degree and angle (Granot & Königl 2003; Lan & Dai 2020; Gill & Granot 2021). This could be the explanation for the fact that the polarization angle was found to change twice, first by around 80∘ and later back again to its original value in GRB 160821A (Sharma et al. 2019). We note that the polarization degree indeed decreases during interval 2, even though the errors are large on the measurements.

A consequence of the results presented in this paper is that only a fraction of GRBs should have bright, late synchrotron pulses because nebula rings are only observed to occur in a fraction of WR stars. Such late prompt synchrotron emission provides diagnostics of the inner parts of the progenitor winds that were emitted a few centuries prior to the GRB explosion.

We thank the anonymous referee for useful suggestions and Dr. Filip Samuelsson for useful discussions. We acknowledge support from the Swedish National Space Agency (131/18 and 2020-00084) and the Swedish Research Council (Vetenskapsrådet, 2018-03513, 2020-00540). S.I. is supported by DST INSPIRE Faculty Scheme (IFA19-PH245). This research made use of the High Energy Astrophysics Science Archive Research Center (HEASARC) Online Service at the NASA/Goddard Space Flight Center (GSFC). In particular, we thank the GBM team for providing the tools and data.

Appendix A
Synchrotron Modeling

We model the emission as fast-cooled synchrotron emission, as described in Aharonian et al. (2010). Specifically, we use the Naima software package (Zabalza 2015) to carry out the calculations of the model spectra. The distribution of electrons with energy e is modeled by a broken power law, with a low-energy ($e < e_{\rm break}$) slope fixed at $\alpha = 2$ (expected for fast cooling synchrotron). In the presence of a population of accelerated electrons, a high-energy power law ($e > e_{\rm break}$) is free to vary and includes an exponential cutoff at high energies, $e_{\rm cutoff}$. For intervals 1 and 3, our initial fits yield posteriors of $p > 10$ and $e_{\rm cutoff}$ tending to merge with $e_{\rm break}$. These results imply that there is no high-energy power law (p) and an $e_{\rm cutoff} > e_{\rm break}$ is not found. Physically, this means that there is no evidence that particle acceleration has taken place and that the electrons are from a heated quasi-Maxwellian distribution. In order to represent such a very narrow electron distribution, we choose to freeze p and $e_{\rm cutoff}$ at large values in intervals 1 and 3. This in turn allows us to get better constraints on all other parameters. We note that after the convolution with the synchrotron kernel the observed spectra from a quasi-Maxwellian distribution and our simplified electron distribution will be indistinguishable. In Table 3 we present the values of all frozen parameters of our model. All fixed parameters are frozen to the same values across the three intervals, with the exception of p and $e_{\rm cutoff}$, which are free in interval 2. Note that we fit for breaks in the electron spectrum, mainly $e_{\rm break}$, which is more commonly parameterized in terms of the comoving electron Lorentz factor, γ. This, in turn, can be translated to where the break lies in the photon spectrum, $h\nu$.

Table 3
List of Parameters of the Synchrotron Model

Parameter	Fixed Values	Unit	Description
$N_{\rm e,0}$	10^{42}	keV^{-1}	Amplitude at the $e_{\rm break}$ of the electron distribution
e_0	1	TeV	Reference point for the electron distribution broken power law
β	10		Sharpness of the high-energy cutoff in the electron distribution
$\rm e_{min}$	0.05	TeV	Minimum electron energy for the electron distribution
$\rm e_{max}$	1000	TeV	Maximum electron energy for the electron distribution
nEed	10		Number of points per decade in energy for the electron energy and distribution arrays
α	2		Power-law index for $e < e_{\rm break}$
p^*	20		Power-law index for $e > e_{\rm break}$
$e_{\rm cutoff}{}^*$	50	TeV	Cutoff energy at higher energies of the electron distribution
$e_{\rm break}$		TeV	Break energy of the electron distribution broken power law
B		Gauss	Isotropic magnetic field strength
norm			Normalization (differential flux at a distance of 1 Mpc)

Note. The values of the parameters which are kept fixed are given. Note that * p and $e_{\rm cutoff}$ are free parameters in interval 2.

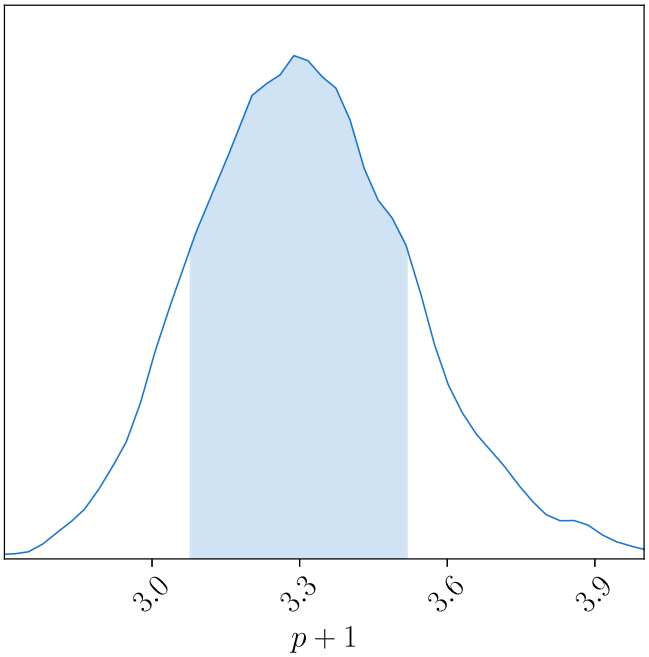

Figure 5. The posterior distribution of the fitted power-law index of the accelerated electron distribution in interval 2. The injected power-law slope p is steepened by unity due to the cooling. The shaded area is the 95% credible region. The fitted value of $p = 2.3 \pm 0.2$ is in line with the robust expectations for particle acceleration in weakly magnetized flows (Sironi et al. 2015).

A.1. Spectral Analysis

The spectral analysis is carried out in the Multi-Mission Maximum Likelihood (3ML) software (Vianello et al. 2015). We implement a Bayesian analysis, in which we evaluate the posterior of our model conditioned on observed data using MultiNest (Feroz et al. 2011) implemented in Python (Buchner 2016). The analysis is carried out using 1000 live points.

The priors for the free parameters in intervals 1 and 3 are given by

$$P(e_{\rm break}) = U(0.05,\ 30)\ ({\rm TeV})$$
$$\log P(B) = U(10^{-1},\ 10^{4})\ ({\rm G})$$
$$\log P({\rm norm}) = U(10^{-2},\ 10^{2}).$$

In addition to these parameters, in interval 2 we also fit for p and $e_{\rm cutoff}$, which are given the following priors

$$P(p) = U(2,\ 20)$$
$$\log P(e_{\rm cutoff}) = U(10^{-1},\ 10^{1})\ ({\rm TeV}).$$

Further, the analysis was carried out using different priors and with different numbers of live points (500 and 2000). From trying both wider and narrower priors on all parameters, we find no significant impact on the results, as long as the priors include the mode of the posterior with some margin. Using 500 live points was sometimes sufficient for convergence, whereas we found no significant difference between using 1000 or 2000 live points. We thus conclude that our results are not sensitive to our choices of priors, and further, our posteriors are sampled satisfactorily.

In Figure 3 we present fits of the model to the data in terms of draws from the posterior distribution plotted together with the observed data in count space. Additionally, the plots also contain the maximum a posteriori (MAP) estimate, corresponding to the mode of the posterior distribution. By visual inspection, there is a decent agreement between the model and the observed data. In the third interval, there was no significant LAT-LLE data. In the LLE energy range, the model predicts a flux well below the detection threshold, consistent with the observations. In order to reach a detection significance of 4σ (the threshold used by the Fermi-LAT collaboration, e.g., Ajello et al. 2019), the model flux in this energy range would need to be doubled.

Figure 4 shows the posteriors for the three intervals together. We include all free parameters in our analyses. Finally, Figure 5 shows the posterior distribution of the fitted power-law index of the accelerated electron distribution in interval 2. The injected power-law slope p is steepened by unity due to the cooling. The fitted value is therefore $p = 2.3 \pm 0.2$.

The emergence of a high-energy flux distribution in interval 2 is very significant. We find highly significant changes in information criteria AIC and BIC (Bayesian Information Criteria) between a fit with and a fit without a high-energy power-law distribution of the electrons: $\Delta{\rm AIC} = 102$ and $\Delta{\rm BIC} = 95$. In this comparison, the parameters $B, e_{\rm break}$, and norm were free to vary. In addition, we also find that the residuals between the best-fit model and the data have a very pronounced wavy structure, which is indicative of the need for an additional component in the spectral model.

A.2. Estimation of the Redshift

The redshift of GRB 160821A is not known. While the determined spectral shape and the identification of the onset of particle acceleration is independent of this fact, the determined energetics and magnetizations will depend on the assumed value. We will assume the value to be $z = 0.4$ based on the following reasoning.

The fluence of GRB 160821A in the range 10 keV–5 GeV is $(1.30 \pm 0.03) \times 10^{-3}\,{\rm erg\,cm^{-2}}$, which makes it among the brightest observed (Sharma et al. 2019). This means that the burst is either very close or, if distant, exceptionally bright. GRBs have a broad distribution of isotropically equivalent energy output, $E_{\rm iso}$, reaching up to $\sim 7 \times 10^{54}$ erg for GRB 160625B (Sharma et al. 2021). Assuming $E_{\rm iso} = 7 \times 10^{54}$ erg for GRB 160821A yields an upper value of the redshift to a modest $z = 1$. On the other hand, there was no associated supernova detection for GRB 160821A. In addition, we searched various optical surveys such as the Sloan Digital Sky Survey (SDSS), Panoramic Survey Telescope and Rapid Response System (Pan-STARRS), as well as radio source surveys of both VLA and GMRT, from the database maintained by the VizieR Catalogue Service and did not find any evidence for the host galaxy at the GRB localization. This led us to the inference that the host galaxy in optical is very faint (R mag > 23.2; Chambers et al. 2016). Following the study of the host galaxies of long GRBs (Hjorth et al. 2012; Jakobsson et al. 2012), the lowest redshift at which a faint long GRB host galaxy with an R mag > 23 that has been detected to date is around $z = 0.4$. Therefore, $z = 0.4$ serves as a lower limit for the redshift in GRB 160821A.

Two further arguments support the lower value of the redshift. First, the highest energy of the LAT photons calculated in the rest fame for GRB 160821A is $E_{\rm max}^{\rm LAT} \sim 4.7(1+z)$ GeV < 10 GeV, which is among the lowest 20% of observed $E_{\rm max}^{\rm LAT}$ values (Ajello et al. 2019). Because there is an observed positive trend between $E_{\rm max}^{\rm LAT}$ and

$E_{\rm iso}$ (Ajello et al. 2019), the low value of $E_{\rm max}^{\rm LAT}$ in GRB 160821A indicates a low value of $E_{\rm iso}$. Second, the late onset time of the afterglow emission (∼185 s) indicates again that $E_{\rm iso}$ should be relatively low (Ghirlanda et al. 2018). Low $E_{\rm iso}$ combined with the measured fluence supports that GRB 160821A is not very distant.

We, therefore, use the estimate of the redshift $z = 0.4$, which, for GRB 160821A, implies a value of $E_{\rm iso} = 7.6 \times 10^{53}$ erg in the gamma rays.[6] Such a value is within the typical range of other LAT-detected GRBs (Racusin et al. 2011; Ajello et al. 2019).

A.3. Derivation of Physical Parameters

We will assume the bulk Lorentz factor, $\Gamma = 300$, and the redshift $z = 0.4$. In order to estimate the values of the magnetic field and the characteristic Lorentz factors of the electrons, we first use the value of the observed cooling break in interval 1, which is given by

$$h\nu_{\rm c1}' = \frac{3q_{\rm e}h}{4\pi m_{\rm e}c}\,\gamma_{\rm c1}^2 B_1 = h\nu_{\rm c1}^{\rm obs}\,\Gamma^{-1}(1+z). \tag{A1}$$

We then set the cooling time to be the width of the time bin, $t_{\rm bin} \sim 10$ s:

$$t_{\rm c}' = \frac{6\pi m_{\rm e}c}{\sigma_{\rm T}}\gamma_{\rm c}^{-1}B^{-2} = t_{\rm c}^{\rm obs}\,\Gamma(1+z)^{-1} \sim 10{\rm s}\,\Gamma(1+z)^{-1}. \tag{A2}$$

Equations (A1) and (A2) together yield the comoving values for $\gamma_{c,1}$ and B_1.

Next, the measured ratio of

$$\frac{h\nu_{\rm c}}{h\nu_{\rm m}} = \left(\frac{\gamma_{\rm c}}{\gamma_{\rm m}}\right)^2, \tag{A3}$$

which gives a value of $\gamma_{\rm m1}$.

Turning over to interval 2, as mentioned above, we will assume that the cooling times are the same in both intervals (the time bins are of similar widths), which is equivalent to the same emission radius, R. Consequently,

$$\frac{t_{c,1}}{t_{c,2}} = \frac{B_2^2\gamma_{c,2}}{B_1^2\gamma_{c,1}} = 1. \tag{A4}$$

This can be combined with

$$\frac{\gamma_{\rm c1}}{\gamma_{\rm c2}} = \left(\frac{h\nu_{\rm c1}}{h\nu_{\rm c2}}\frac{B_2}{B_1}\right)^{1/2} \tag{A5}$$

from Equation (A1), which gives, with Equation (A4),

$$\frac{B_2}{B_1} = \left(\frac{h\nu_{\rm c1}}{h\nu_{\rm c2}}\right)^{1/3}, \tag{A6}$$

giving B_2 and

$$\frac{\gamma_{\rm c2}}{\gamma_{\rm c1}} = \left(\frac{h\nu_{\rm c2}}{h\nu_{\rm c1}}\right)^{2/3}, \tag{A7}$$

giving $\gamma_{\rm c2}$.

From Equation (A1) we similarly have that

$$\frac{h\nu_{\rm c2}}{h\nu_{\rm m2}} = \left(\frac{\gamma_{\rm c2}}{\gamma_{\rm m2}}\right)^2, \tag{A8}$$

which gives the value of $\gamma_{\rm m2}$.

For the energy flux at the spectral peak ($h\nu_{\rm c}$) with $F_{\nu,{\rm c1}} \equiv F_\nu(h\nu_{\rm c1})$ we have

$$\frac{F_{\nu,{\rm c1}}}{F_{\nu,{\rm c2}}} = \frac{P_{\nu,{\rm c1}}N_{e1}}{P_{\nu,{\rm c2}}N_{e2}}, \tag{A9}$$

which, because $P_{\nu,c} \propto B$, combined with Equation (A6), gives

$$\frac{N_{e1}}{N_{e2}} = \frac{F_{\nu,{\rm c1}}}{F_{\nu,{\rm c2}}}\left(\frac{h\nu_{\rm c1}}{h\nu_{\rm c2}}\right)^{1/3}. \tag{A10}$$

The number of electrons is (approximate to a factor of a few)

$$N_{e1} \sim \frac{4\pi d_L^2}{(1+z)}\frac{q}{m_{\rm e}c^2\sigma_{\rm T}}\frac{F_{\nu,{\rm c1}}}{B_1\Gamma}. \tag{A11}$$

From this we can calculate the magnetization, which is defined as the ratio of the Poynting flux and the matter enthalpy flux, and becomes in the downstream of the shock

$$\sigma_{\rm d}(r) = \frac{B'^2}{4\pi\Gamma n'(r)\,m_{\rm p}c^2}, \tag{A12}$$

where $n'(r)$ is the comoving number density of the radiating electrons at radius r. Both n' and B' are determined in the downstream, where the energy has been dissipated. The $N_{\rm e}$ electrons radiate from the volume $\pi(r/\Gamma)^2\Delta r'$, where $\Delta r' \sim ct'_{\rm c}/3$. Therefore,

$$n' = \frac{3N_{\rm e}\Gamma^2}{\pi r^2 ct'_c} \tag{A13}$$

and

$$\sigma_{\rm d} = \frac{B'^2\,t'_{\rm c}\,r^2}{12m_{\rm p}c\,N_{\rm e}\Gamma^3} = \frac{B'^2\,t_{\rm c}^{\rm obs}\,r^2}{12m_{\rm p}c\,N_{\rm e}\Gamma^2(1+z)}. \tag{A14}$$

Finally, we assume that the large-scale ordered magnetic field is oriented predominantly transverse to the shock normal (Medvedev & Loeb 1999; Frederiksen et al. 2004; Pelletier et al. 2017). While the transverse field is largely amplified due to the compression across the shock, any parallel component of the field remains unchanged. The latter component will therefore be largely subdominant just behind the shock (Granot & Königl 2003). In such a case, the magnetization in the upstream and downstream is largely similar to each other, $\sigma_{\rm d} \sim 3\sigma_{\rm u}$ (e.g., Lemoine & Pelletier 2010).

Appendix B
Onset of Particle Acceleration and Magnetization

A detection of the onset of particle acceleration could indicate that the critical value of the magnetization $\sigma_{\rm c}$ has been reached and therefore this value can be compared to the observed magnetization, $\sigma_{\rm d}$. The critical value $\sigma_{\rm c}$ is given in the upstream of the shock as $\Gamma_{\rm r}^2\sigma_{\rm c,\,u}\chi_{\rm e}^{-1} \sim 1$, where $\Gamma_{\rm r}$ is the relative Lorentz factor across the shock, and $\chi_{\rm e} \sim 0.1$ is the fraction of shock energy carried by the accelerated electrons (Lemoine et al. 2013). For a transverse shock, the magnetization in the upstream and downstream are largely

[6] The isotropic burst energy estimate in this Letter uses the standard ΛCDM cosmology, with cosmological parameters, $H_0 = 67.4 \pm 0.5$ km s^{-1} Mpc^{-1}, $\Omega_{\rm vac} = 0.685$ and $\Omega_m = 0.315$ (Planck Collaboration et al. 2020).

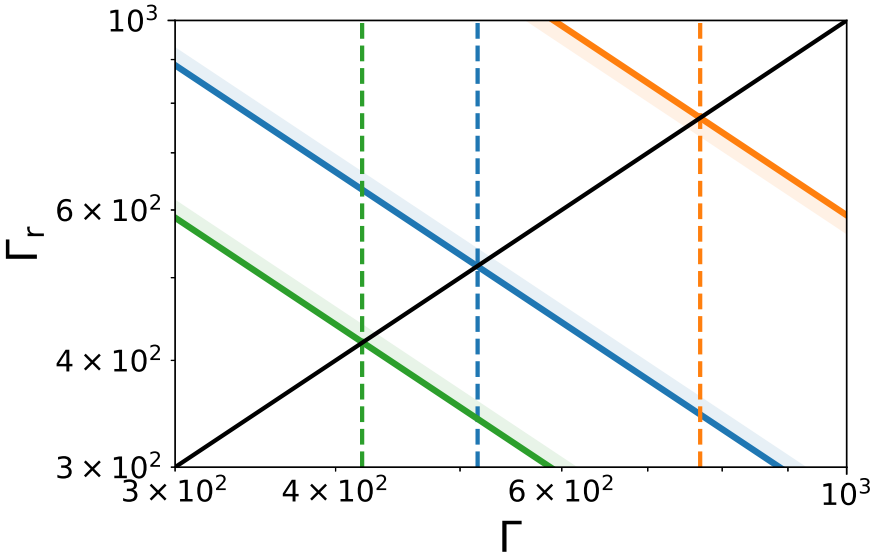

Figure 6. The relative Lorentz factor Γ_r across the shock vs. the bulk Lorentz factor, Γ. The colored lines are given by $\Gamma_r = 0.55\sigma_d^{-1/2}(\Gamma)$, where $\sigma_d(\Gamma)$ is the measured magnetization for different Γ. The lines are for the three intervals in GRB 160820A (same colors as in Figure 2). The black line is for $\Gamma_r = \Gamma$; therefore, only parameter values below this line are allowed. The lines cross each other at $\Gamma = 420$, 510, and 770, as marked by the dashed lines. This gives the estimate of the Lorentz factor to be $420 < \Gamma < 770$. A redshift of $z = 0.4$ is assumed.

Table 4
Derived Physical Parameters for $\Gamma = 595$ and $z = 0.4$

Time Intervals	γ_c (10^5)	γ_m (10^5)	B (Gauss)	R_{dyn} (10^{17} cm)	N_e (10^{49})	σ (10^{-7})
Interval 1	$1.06^{+0.08}_{-0.08}$	$7.5^{+0.5}_{-0.5}$	$1.31^{+0.05}_{-0.05}$	8.5	$2.74^{+0.06}_{-0.05}$	$15.2^{+1.4}_{-1.5}$
Interval 2	$1.41^{+0.06}_{-0.07}$	$5.2^{+0.8}_{-0.8}$	$1.14^{+0.03}_{-0.03}$	〃	$10.2^{+0.1}_{-0.1}$	$3.0^{+0.2}_{-0.2}$
Interval 3	$0.53^{+0.04}_{-0.05}$	$5.0^{+0.5}_{-0.5}$	$1.85^{+0.10}_{-0.07}$	〃	$2.40^{+0.07}_{-0.06}$	$34.5^{+3.8}_{-4.7}$

Note. The error intervals are reported with a 95% confidence interval and estimated as Bayesian credible intervals. The critical value of the magnetization is $\sigma_c = 8.5 \times 10^{-7}$.

similar and, therefore, the condition for Fermi acceleration becomes $\sigma_d \lesssim \sigma_{c,d} = 0.3\Gamma_r^{-2}$.

A comparison between the measured magnetization σ_d and the critical value $\sigma_{c,d}$ for interval 2 (the interval with particle acceleration) gives an upper limit of $\Gamma_r \leqslant 0.55\sigma_d^{-1/2}(\Gamma)$. For the other two intervals, the requirement gives lower limits. Figure 6 illustrates this for the three intervals in GRB 160821A. Because Γ_r by necessity is smaller than Γ, this analysis gives a lower range of the estimated bulk Lorentz factor of $420 \lesssim \Gamma \lesssim 770$ (assuming redshift $z = 0.4$).

The range of Lorentz factors is consistent with the values estimated from the general correlation between E_{iso} and Γ found from afterglow measurements (Liang et al. 2010): For the estimated value of $E_{iso} \sim 6.9 \times 10^{53}$ erg for GRB 160821A (Appendix A.2), the expected range is $300 \lesssim \Gamma \lesssim 900$. We note that such large values of Γ are also typically found for synchrotron fits in GRBs using other methods to determine its value (Kumar & McMahon 2008; Beniamini & Piran 2013, 2014; Iyyani et al. 2016; Burgess et al. 2020). Finally, the physical parameter values from the synchrotron fit assuming the averaged value over the Lorentz factor range, $\Gamma = 595$, are shown in Table 4.

We also note that the high-energy slopes of synchrotron spectra in other GRBs are typically softer than what are expected from Fermi acceleration (Goldstein et al. 2012; Yu et al. 2016; Ravasio et al. 2018; Yu et al. 2019; Burgess et al. 2020; Li et al. 2021). This indicates that σ_c must be low in order for the magnetization of the GRB to inhibit particle acceleration. This in its turn again requires that Γ_r must be large for these bursts (Lemoine & Pelletier 2010), suggesting once more an external-shock origin of such emission.

ORCID iDs

Felix Ryde https://orcid.org/0000-0002-9769-8016
Shabnam Iyyani https://orcid.org/0000-0002-2525-3464
Björn Ahlgren https://orcid.org/0000-0003-4000-8341
Asaf Pe'er https://orcid.org/0000-0001-8667-0889
Vidushi Sharma https://orcid.org/0000-0002-4394-4138
Christoffer Lundman https://orcid.org/0000-0002-0642-1055
Magnus Axelsson https://orcid.org/0000-0003-4378-8785

References

Abdo, A. A., Ackermann, M., Arimoto, M., et al. 2009, Sci, 323, 1688
Acuner, Z., & Ryde, F. 2018, MNRAS, 475, 1708
Aharonian, F. A., Kelner, S. R., & Prosekin, A. Y. 2010, PhRvD, 82, 043002
Ajello, M., Arimoto, M., Axelsson, M., et al. 2019, AJ, 878, 52
Atwood, W. B., Abdo, A. A., Ackermann, M., et al. 2009, ApJ, 697, 1071
Axelsson, M., Baldini, L., Barbiellini, G., et al. 2012, ApJL, 757, L31
Beloborodov, A. M. 2000, ApJL, 539, L25
Beloborodov, A. M. 2017, ApJ, 838, 125
Beniamini, P., & Piran, T. 2013, ApJ, 769, 69
Beniamini, P., & Piran, T. 2014, MNRAS, 445, 3892
Bhalerao, V., Kumar, V., Bhattacharya, D., Rao, A. R., & Vadawale, S. 2016, GCN, 19867, 1
Buchner, J. 2016, PyMultiNest: Python interface for MultiNest, Astrophysics Source Code Library, ascl:1606.005
Burgess, J. M., Bégué, D., Greiner, J., et al. 2020, NatAs, 4, 174
Burgess, J. M., Preece, R. D., Connaughton, V., et al. 2014, ApJ, 784, 17
Chambers, K. C., Magnier, E. A., Metcalfe, M., et al. 2016, arXiv:1612.05560
Chu, Y. H. 1981, ApJ, 249, 195
Crowther, P. A. 2007, ARA&A, 45, 177
Derishev, E. V. 2017, in AIP Conf. Ser. 1792, 6th Int. Symp. on High Energy Gamma-Ray Astronomy (Melville, NY: AIP), 020005

Derishev, E. V., Aharonian, F. A., Kocharovsky, V. V., & Kocharovsky, V. V. 2003, PhRvD, 68, 043003
Derishev, E. V., & Piran, T. 2016, MNRAS, 460, 2036
Feroz, F., Hobson, M. P., & Bridges, M. 2011, MultiNest: Efficient and Robust Bayesian Inference, Astrophysics Source Code Library, ascl:1109.006
Frederiksen, J. T., Hededal, C. B., Haugbølle, T., & Nordlund, Å 2004, ApJL, 608, L13
Ghirlanda, G., Nappo, F., Ghisellini, G., et al. 2018, A&A, 609, A112
Gill, R., & Granot, J. 2021, MNRAS, 504, 1939
Gill, R., Granot, J., & Kumar, P. 2020, MNRAS, 491, 3343
Goldstein, A., Burgess, J. M., Preece, R. D., et al. 2012, ApJS, 199, 19
Granot, J., & Königl, A. 2003, ApJL, 594, L83
Hjorth, J., Malesani, D., Jakobsson, P., et al. 2012, ApJ, 756, 187
Hu, Y.-D., Liang, E.-W., Xi, S.-Q., et al. 2014, AJ, 789, 145
Iyyani, S., Ryde, F., Burgess, J. M., Pe'er, A., & Bégué, D. 2016, MNRAS, 456, 2157
Jakobsson, P., Hjorth, J., Malesani, D., et al. 2012, in IAU Symp. 279, Death of Massive Stars: Supernovae and Gamma-Ray Bursts, ed. P. Roming, N. Kawai, & E. Pian (Cambridge: Cambridge Univ. Press), 187
Johnson, H. M., & Hogg, D. E. 1965, ApJ, 142, 1033
Keshet, U., Katz, B., Spitkovsky, A., & Waxman, E. 2009, ApJL, 693, L127
Kirk, J. G., & Reville, B. 2010, ApJL, 710, L16
Kobayashi, S., Piran, T., & Sari, R. 1997, ApJ, 490, 92
Kobayashi, S., & Sari, R. 2001, ApJ, 551, 934
Kumar, P., & McMahon, E. 2008, MNRAS, 384, 33
Lan, M.-X., & Dai, Z.-G. 2020, ApJ, 892, 141
Lazzati, D., & Perna, R. 2007, MNRAS, 375, L46
Lemoine, M. 2013, MNRAS, 428, 845
Lemoine, M., Li, Z., & Wang, X.-Y. 2013, MNRAS, 435, 3009
Lemoine, M., & Pelletier, G. 2010, MNRAS, 402, 321
Lemoine, M., & Pelletier, G. 2011, MNRAS, 417, 1148
Li, L. 2020, ApJ, 894, 100
Li, L., Ryde, F., Pe'er, A., Yu, H.-F., & Acuner, Z. 2021, ApJS, 254, 35
Liang, E.-W., Yi, S.-X., Zhang, J., et al. 2010, ApJ, 725, 2209
Marston, A. P. 1997, ApJ, 475, 188
Medvedev, M. V., & Loeb, A. 1999, ApJ, 526, 697
Meegan, C., Lichti, G., Bhat, P. N., et al. 2009, ApJ, 702, 791
Mészáros, P., Ramirez-Ruiz, E., Rees, M. J., & Zhang, B. 2002, ApJ, 578, 812
Oganesyan, G., Nava, L., Ghirlanda, G., & Celotti, A. 2017, ApJ, 846, 137
Oganesyan, G., Nava, L., Ghirlanda, G., Melandri, A., & Celotti, A. 2019, A&A, 628, A59
Pe'er, A., Long, K., & Casella, P. 2017, ApJ, 846, 54
Pe'er, A., & Wijers, R. A. M. J. 2006, ApJ, 643, 1036
Pelletier, G., Bykov, A., Ellison, D., & Lemoine, M. 2017, SSRv, 207, 319
Pereyra, M., Fraija, N., Watson, A. M., et al. 2021, arXiv:2111.15168
Planck Collaboration, Aghanim, N., & Akrami, Y. 2020, A&A, 641, A6
Racusin, J. L., Oates, S. R., Schady, P., et al. 2011, ApJ, 738, 138
Ravasio, M. E., Ghirlanda, G., Nava, L., & Ghisellini, G. 2019, A&A, 625, 60
Ravasio, M. E., Oganesyan, G., Ghirlanda, G., et al. 2018, A&A, 613, A16
Rees, M. J., & Mészáros, P. 1992, MNRAS, 258, 41
Rees, M. J., & Mészáros, P. 1994, ApJL, 430, L93
Samuelsson, F., Lundman, C., & Ryde, F. 2022, ApJ, 925, 65
Sari, R., Piran, T., & Narayan, R. 1998, ApJL, 497, L17
Sharma, V., Iyyani, S., & Bhattacharya, D. 2021, ApJL, 908, L2
Sharma, V., Iyyani, S., Bhattacharya, D., et al. 2019, ApJL, 882, L10
Sironi, L., Keshet, U., & Lemoine, M. 2015, SSRv, 191, 519
Sironi, L., & Spitkovsky, A. 2011, ApJ, 726, 75
Sironi, L., Spitkovsky, A., & Arons, J. 2013, ApJ, 771, 54
Spada, M., Panaitescu, A., & Mészáros, P. 2000, ApJ, 537, 824
Spitkovsky, A. 2008, ApJL, 682, L5
Stanbro, M., & Meegan, C. 2016, GCN, 19835, 1
Stock, D. J., & Barlow, M. J. 2010, MNRAS, 409, 1429
Tavani, M. 1996, ApJ, 466, 768
Toalá, J. A., & Guerrero, M. A. 2013, A&A, 559, A52
Vianello, G., Lauer, R., Younk, P., et al. 2015, ICRC (The Hague), 34, 1042
Wijers, R. A. M. J., & Galama, T. J. 1999, ApJ, 523, 177
Yu, H.-F., Dereli-Bégué, H., & Ryde, F. 2019, ApJ, 886, 20
Yu, H.-F., Preece, R. D., Greiner, J., et al. 2016, A&A, 588, A135
Zabalza, V. 2015, ICRC (The Hague), 34, 922
Zhang, B. B., Zhang, B., Castro-Tirado, A. J., et al. 2018, NatAs, 2, 69